Japanese Journal of Applied Physics

The Japan Society of Applied Physics

RAPID COMMUNICATION

Electrically tunable temporal imaging in a graphene-based waveguide

To cite this article: Peng Xie *et al* 2019 *Jpn. J. Appl. Phys.* **58** 050914

Japanese Journal of Applied Physics **58**, 050914 (2019) **RAPID COMMUNICATION**
https://doi.org/10.7567/1347-4065/ab0c52

Electrically tunable temporal imaging in a graphene-based waveguide

Peng Xie[1,2,3,4], Yu Wen[5], Zishen Wan[2,4*], Xinyu Wang[1,3], Jiarui Liu[6], Wenqiang Yang[1,3], Xiaofeng Li[1], and Yishan Wang[1,3]

[1]*State Key Laboratory of Transient Optics and Photonics, Xi'an Institute of Optics and Precision Mechanics, Chinese Academy of Sciences, Xi'an 710119, People's Republic of China*
[2]*Department of Mechanical Engineering, Massachusetts Institute of Technology, Cambridge 02139, United States of America*
[3]*University of Chinese Academy of Sciences, Beijing 100049, People's Republic of China*
[4]*School of Engineering and Applied Sciences, Harvard University, Cambridge 02138, United States of America*
[5]*National University of Defence Technology, Changsha, 410073, People's Republic of China*
[6]*Sun Yat-Sen University, Guangzhou 510000, People's Republic of China*

*E-mail: zishenwan@g.harvard.edu

Received February 14, 2019; revised March 1, 2019; accepted March 4, 2019; published online April 16, 2019

We propose an electrically tunable temporal imaging system (TIS) based on four-wave mixing in a dispersion engineered graphene-based waveguide, which could realize a magnification factor of 1000× for a signal consisting of two 100-fs-wide pulses separated by 500 fs and a large working bandwidth of about 700 nm. The TIS was analyzed by solving the couple-mode equations in detail. It was demonstrated that the working wavelength range could be tuned via a small disturbed bias voltage applied to the graphene layer without changing the geometric structure of the waveguide. These results provide attractive insights for potential applications in integrated optics and optical communications.

In recent years, temporal imaging based on the concept of space–time duality has attracted increasing attention for various applications,[1–3] such as time magnification,[4,5] timing jitter reduction,[6] ultrafast optical signal measurements[7] and bandwidth manipulation of quantum light.[8] A temporal imaging system (TIS) consists of three parts including an input dispersion module, a time lens and an output dispersion module.[9–11] The time lens plays an important role in the TIS, which is equivalent to a spatial lens imparting a quadratic phase to the input optical waveform.[3–5] The most straightforward way to realize a time lens is based on an electro-optical phase modulator (EOPM) driven by a sinusoidal radio frequency signal.[12–14] However, this method is limited by the modulation bandwidth and the maximum phase shift of the EOPM, which is not capable of imparting a larger quadratic phase to the input signal.[5,15] In comparison to an EOPM, using nonlinear parametric processes such as sum-frequency or differential-frequency generation, cross-phase modulation and four-wave mixing (FWM), is a promising route to breaking these limitations by providing a platform for all-optical phase modulation.[16,17] Specifically, the approach exploiting FWM is applicable to most materials and is suitable for fundamental CMOS compatible platforms, such as silica glass, silicon or silicon nitride,[9] which exhibits attractive potential for creating a chip-TIS. Moreover, silicon-based waveguides are popular nonlinear media for FWM, which exploits the large Kerr parameter, tight confinement of the optical mode, and instantaneous response time for high-speed operation.[18] These advantages could facilitate the development of signal-processing systems to photonics networks, for design flexibility and the mature fabrication technology. One drawback to traditional silicon-based waveguides is that the properties are determined as the geometric structure is fixed. Thus, graphene, a two-dimensional substance of carbon, entered researchers' sights for its CMOS compatibility and unique optoelectronics properties,[19,20] which provide the possibility of designing devices with tunable properties at a fixed structure. Moreover, graphene exhibits large nonlinear refractive index (10^{-7} cm^2 W^{-1}), and is an attractive candidate material for nonlinear photonic devices, which could be used for creating novel devices with high nonlinear coefficient and low loss. The properties of devices combining silicon-based materials with graphene could be changed by applying extra bias voltage to the graphene layer,[21,22] exhibiting pivotal potential to develop a nonlinear parametric system with high conversion efficiency under low pump.

In this paper, a dispersion engineered graphene-based waveguide is proposed to realize an electrically tunable TIS. A wide bandwidth of about 700 nm in the near infrared region and a large magnification factor of 1000× for fs pulses were achieved. Moreover, the tunability of the effective working wavelength range was demonstrated via extra bias voltage loading to the graphene layer. This electrically tunable chip-TIS exhibits significant potential for all-optical communication.

Silicon-on-insulator (SOI) waveguides are widely used in devices for their design flexibility, which can take the form of channel waveguides, ridge waveguides, photonic crystal waveguides, or slot waveguides. Moreover, mature CMOS technology applied to SOI waveguides makes them an attractive platform for photonic integration.[2] In recent years, combining SOI with graphene has attracted increasing attention in the device field, which could make full use of their unique advantages.[23–28] Specifically, the optical conductivity σ of graphene could be controlled through adjusting bias voltage or chemical doping,[29–31] which has a significant influence on the properties of graphene-related waveguides and raises the possibility of developing multifunctional devices. Loading bias voltage to the graphene layer is the most convenient way to obtain an acceptable value, which can be calculated using the Kubo formula:[32,33]

$$\begin{aligned}\sigma(\omega, \mu_c, \Gamma, T) &= \sigma_{\text{intra}} + \sigma_{\text{inter}} \\ &= \frac{-ie^2}{\pi\hbar^2(\omega + i2\Gamma)}\left[\int_0^\infty \varepsilon\left(\frac{\partial f_d(\varepsilon)}{\partial\varepsilon} - \frac{\partial f_d(-\varepsilon)}{\partial\varepsilon}\right)d\varepsilon\right] - \frac{ie^2(\omega + i2\Gamma)}{\pi\hbar^2} \\ &\quad \times \left[\int_0^\infty \frac{f_d(-\varepsilon) - f_d(\varepsilon)}{(\omega + i2\Gamma)^2 - 4(\varepsilon/\hbar)^2}d\varepsilon\right] \end{aligned} \quad (1)$$

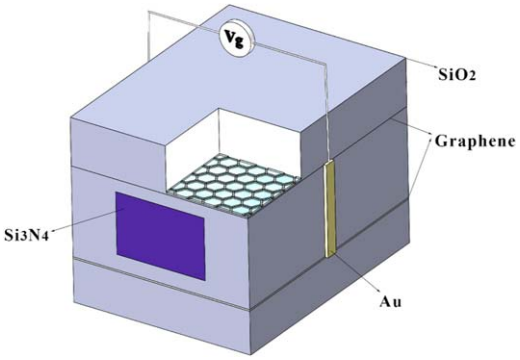

Fig. 1. (Color online) (a) Three-dimensional structure of a graphene-covered silicon nitride waveguide.

$$\sigma_{\text{intra}} = -j\frac{e^2 k_B T}{\pi\hbar^2(\omega - j2\Gamma)} \times \left[\frac{\mu_c}{k_B T} + 2\ln(e^{-\mu_c/k_B T} + 1)\right] \quad (2)$$

$$\sigma_{\text{inter}} = -j\frac{e^2}{4\pi\hbar}\ln\left(\frac{2|\mu_c| - (\omega - j2\Gamma)\hbar}{2|\mu_c| + (\omega - j2\Gamma)\hbar}\right) \quad (3)$$

where ω is the angular frequency of the plasmon, e and K_B are the electron charge and the Boltzmann constant respectively, T is the temperature, $\hbar$ is the reduced Planck constant, μ_c is the chemical potential, τ is the electron momentum relaxation time, and Γ is a phenomenological scattering rate. For the electric field, the chemical potential μ_c can be defined as

$$|\mu_c| = \hbar\nu_F\sqrt{\pi|\eta(V_g - V_{\text{Dirac}})|} \quad (4)$$

where $\eta \approx 9 \times 10^{16}\,\text{m}^{-1}\,\text{V}^{-2}$, V_{Dirac} represents the voltage offset of Dirac fermions in graphene, and the expression $|V_g - V_{\text{Dirac}}|$ can be considered the biased voltage V_{biased}, where V_g is the extra voltage which is applied to the graphene layer in practice. The optical conductivity of graphene could be modified dynamically by chemical potential, equivalent to biased voltage as presented in Eq. (4), which could contribute to the variation of the effective refractive index of a graphene-related waveguide relating to the optimization of light confinement, nonlinearity coefficient and second-order dispersion of the waveguide.[34,35] Based on this theory, we have proposed a novel graphene-covered silicon nitride waveguide, as shown in Fig. 1.

Silicon nitride is chosen as the core material of the waveguide for its high nonlinear refractive index of $n_2 = 2.6 \times 10^{-19}\,\text{m}^2\,\text{W}^{-1}$ and its negligible two photon absorption and associated free carrier effects in the near infrared region. Compared with a conventional silicon waveguide, it could promote the conversion efficiency and avoid the distortion of pulses investigated in it.[36] The core material is surrounded by two graphene layers and the additional bias voltage is applied to the graphene. The two graphene layers remain monolayer and present the same width and thickness, which are $w = 4$ μm and $h = 0.34$ nm, respectively. The waveguide is encased in silica, which is the cladding material. As is well known, second-order dispersion plays an important role in the FWM process, which is directly related to the phase-matching among the interacting waves.[37]

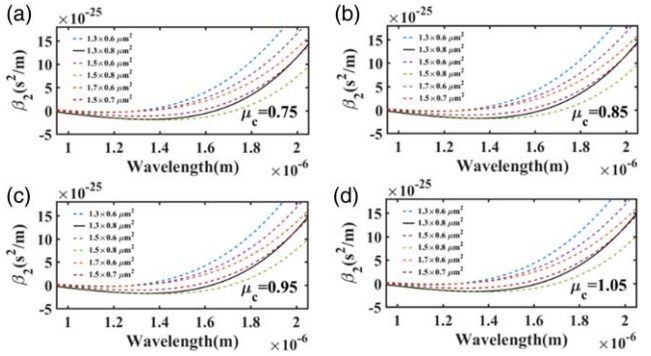

Fig. 2. (Color online) Second-order dispersion characteristics with different dimensions of the core material of a graphene-based waveguide under different bias voltages.

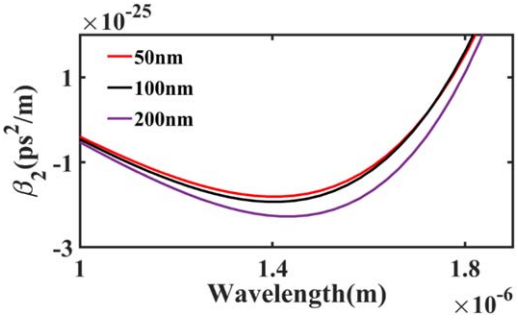

Fig. 3. (Color online) The dispersion characteristics of the waveguide under different gaps between the graphene and the silicon nitride.

An efficient FWM process only occurs after the phase-matching condition is realized, which determines the efficient working wavelength and working bandwidth. Therefore, the second-order dispersion must be carefully designed by controlling the structural shape. The dispersion characteristics with different dimensions of the core material of the graphene-covered silicon nitride waveguide under different chemical potentials (equivalent to bias voltages) are analyzed by the finite-element method, which is depicted in Fig. 2. According to the results of numerical simulation, we can see the variation of dispersion curves and zero dispersion wavelengths (ZDWs). The bandwidth between two ZDWs means the potential working wavelength, which could realize phase-matching. On the other hand, the waveguide with flat dispersion is convenient for achieving an efficient nonlinear process with low pump power. Taking these into consideration, the optimal width and height of the core material are set as $w_{\text{core}} = 1.3$ μm and $h_{\text{core}} = 0.8$ μm, respectively. Moreover, we have explored the influence of different gaps between the graphene and the silicon nitride on second-order dispersion, which is shown in Fig. 3. There are two graphene layers, to which are applied a common bias voltage. It is a fact that the two layers work independently. The gap between the graphene layer and the core material has an important impact on the performance of a graphene-related waveguide. Finally, the gap distance between the graphene and the silicon nitride is determined to be 100 nm after considering bandwidth, dispersion characteristics and practical feasibility factors. All of the size or gap distance values are optimized by numerical simulation using the finite-element method. The TM mode at 1550 nm of the graphene-based waveguide is

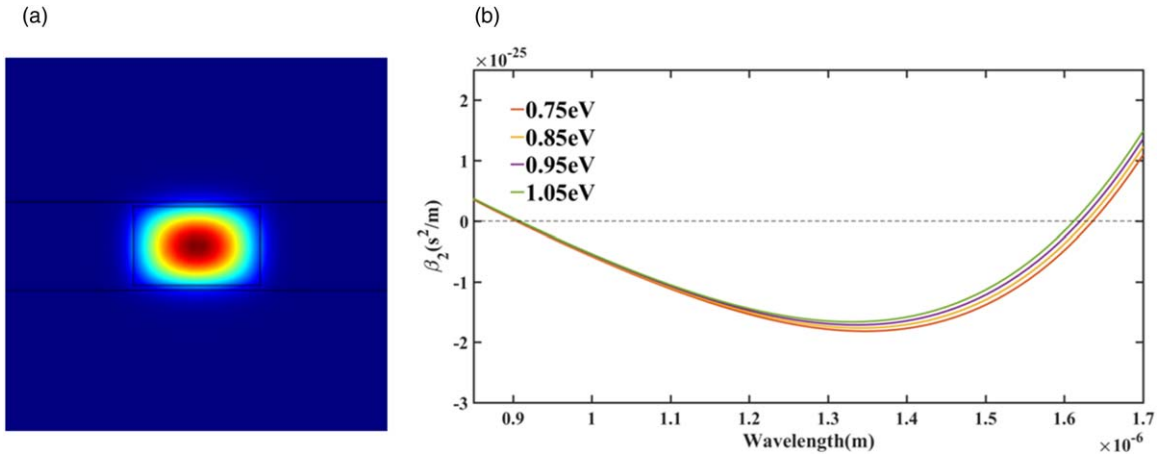

Fig. 4. (Color online) (a) TM mode at 1550 nm for the graphene-based waveguide. (b) Second-order dispersion for different bias voltages.

shown in Fig. 4(a) and the second-order dispersion of the waveguide under different bias voltages is shown in Fig. 4(b). It is found that most of the light is confined in the core region and the second-order dispersion curve is flat with an amplitude close to zero, which means that it is easy to realize phase-matching in the waveguide in a nonlinear parametric process with low threshold. Furthermore, the ZDW varies with different bias voltages, giving promising potential for tuning the working wavelength range. As is shown in Fig. 5, the ZDW is changed by more than 50 nm under small disturbed bias voltage. Moreover, the bandwidth between two ZDWs exceeds 700 nm as shown in Fig. 4(b) and, according to the rules of FWM, the phase-matching could be realized in the wavelength range. This could be regarded as a potential working bandwidth of about 700 nm, which means that FWM could be effectively realized when signal and pump are located inside the wavelength range. Such devices with large bandwidth have been a hot research topic and have attracted much attention in recent years for applications in the optics communication field. As with second-order dispersion, the nonlinearity coefficient associated with the effective mode area also has significant effects on the nonlinear parametric processes. Nonlinearity coefficient γ and effective mode area A_{eff} are crucial parameters of waveguides, which are calculated by the following equations[38)]

$$\gamma = \frac{2\pi n_2}{\lambda A_{\text{eff}}} \tag{5}$$

$$A_{\text{eff}} = \frac{\left[\int\int_{-\infty}^{\infty} |F(x,y)|^2 dxdy\right]^2}{\int\int_{-\infty}^{\infty} |F(x,y)|^4 dxdy} \tag{6}$$

where n_2 is nonlinear refractive index, $F(x, y)$ is the profile of the field and λ is the wavelength. The relationship between nonlinearity coefficient, effective mode area and wavelength is presented in Fig. 6.

FWM has attracted tremendous research interest in optical parametric amplification, wavelength conversion, and optical parametric oscillation due to its practicability for CMOS compatible platforms in the field of integrated optics. Here, we focus on the degenerate FWM, which involves two pump

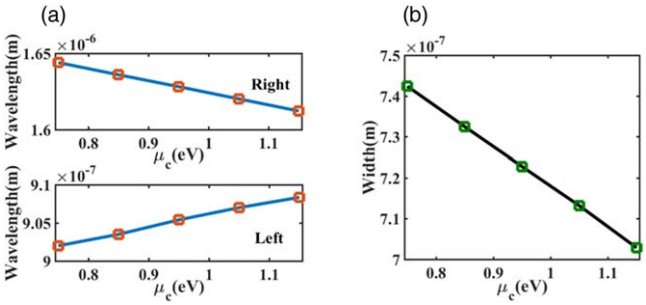

Fig. 5. (Color online) (a) ZDWs for different bias voltages. (b) Bandwidth for different bias voltages.

photons at angular frequency ω_{p} passing their energy to a signal wave at angular frequency ω_{s} and an idler wave at angular frequency ω_{i}, as the relation $2\omega_{\text{p}} = \omega_{\text{s}} + \omega_{\text{i}}$ holds. Phase-matching among the interacting waves is required in the FWM process, and the phase-mismatch is defined as

$$\Delta k = \Delta\beta + 2\gamma_{\text{p}} p_{\text{p}}$$

where $\Delta\beta = k_{\text{s}} + k_{\text{i}} - 2k_{\text{p}}$ is the linear part of the phase-mismatch, and k_{p}, k_{s}, and k_{i} represent the propagation constants of the pump, signal, and idler waves, respectively. The second term is the nonlinear part, where γ_{p} is the effective nonlinearity of the waveguide, and p_{p} is the pump power. Efficient FWM occurs when the phase-matching condition satisfies the relation $\Delta K = 0$. Since the nonlinear part $(2\gamma_{\text{p}} p_{\text{p}})$ is positive, the pump pulse should be located in the anomalous dispersion region to achieve phase-matching.[37)]

Based on this principle and the proposed graphene-related waveguide with tunable dispersion, an electrically tunable TIS is investigated and the FWM process is analyzed using coupled wave equations.[38)] A schematic of the TIS is presented in Fig. 7, which mainly consists of an input dispersive medium, a time lens, a band-pass filter and an output dispersive medium.

A quadratic phase $\varnothing_f(t)$ is imparted to the signal, which determines the focal length of the time lens

$$\varnothing_{\text{f}}(t) = -\frac{t^2}{2\varnothing''_{\text{f}}} \tag{7}$$

where $\varnothing''_{\text{f}}$ is the focal group-delay dispersion (GDD) associated with the lens and is equal to the inverse of the second derivative of the phase. The dispersive elements before and

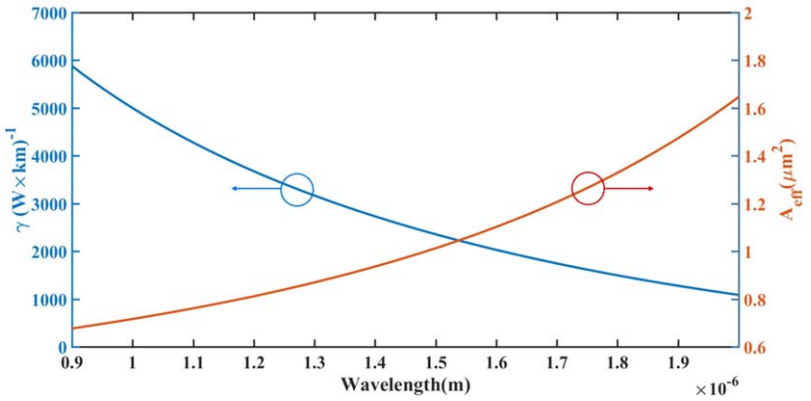

Fig. 6. (Color online) The relationship between nonlinearity coefficient, effective mode area and wavelength.

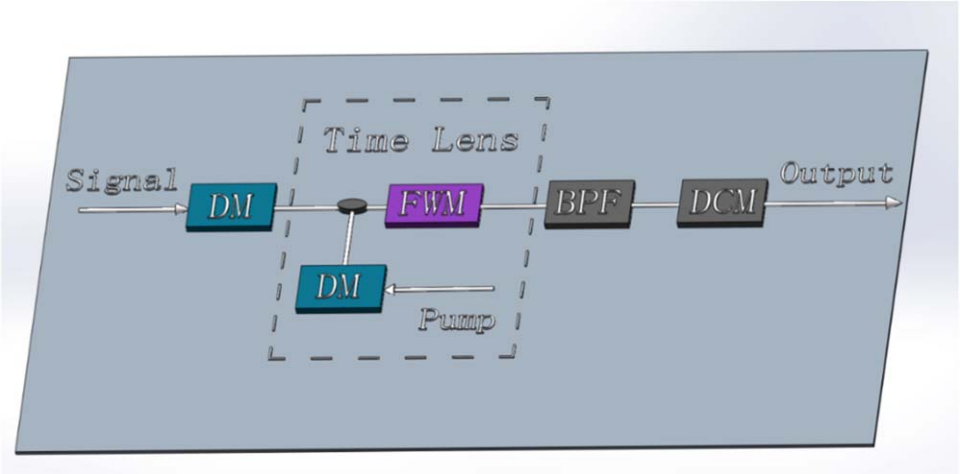

Fig. 7. (Color online) A schematic of the TIS based on FWM in a graphene-related waveguide. DM: dispersion medium; BPF: band-pass filter; DCM: dispersion compensation medium.

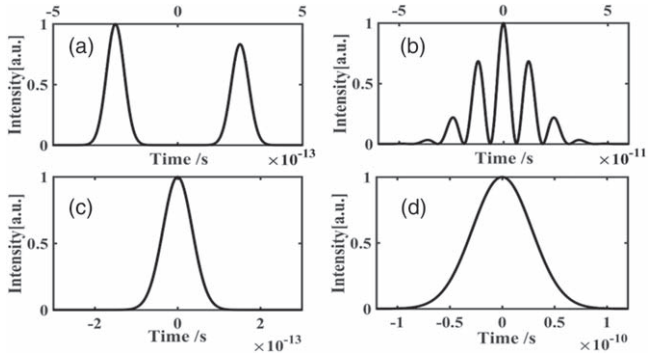

Fig. 8. (a) Temporal waveform of the input signal. (b) Temporal waveform of the input signal through the dispersive element. (b) Temporal waveform of the pump. (d) Temporal waveform of the pump through the dispersive element.

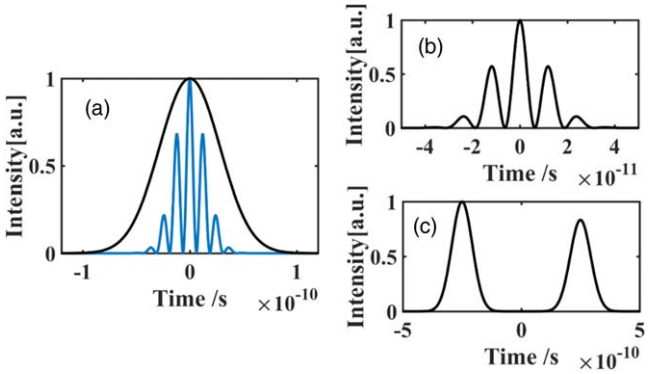

Fig. 9. (Color online) (a) Temporal waveform of the input signal and pump through the dispersive element. (b) Temporal waveform of the idler. (c) Temporal waveform of the output signal.

after the lens are characterized by their GDD parameters $\varnothing_1''$ and $\varnothing_2''$, which can be provided by single mode fiber or fiber Bragg grating. The relationship, analogous to the one used for a spatial lens, describing this imaging system is that

$$\frac{1}{\varnothing_1''} + \frac{1}{\varnothing_2''} = \frac{1}{\varnothing_f''}. \tag{8}$$

In an analogy with spatial imaging, the output waveform will have the same features as the input but scaled by a magnification factor

$$M = -\frac{\varnothing_2''}{\varnothing_1''}. \tag{9}$$

The inverse relationship of the spectral and temporal magnification is a consequence of the scaling property of the Fourier transform.[5)]

In this work, dispersive elements of the signal and pump are provided by a dispersion module equivalent to 100 m and 200 m spools of standard fiber, respectively. The input signal

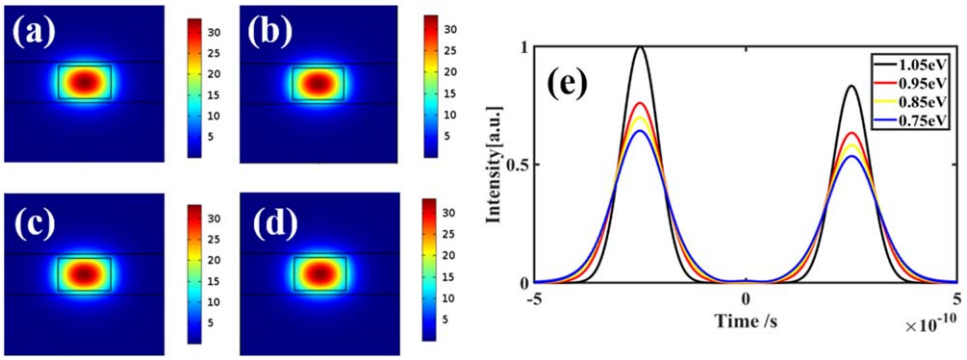

Fig. 10. (Color online) (a)–(d) TM mode at 1550 nm for the waveguide under 0.75 eV, 0.85 eV, 0.95 eV, and 1.05 eV, respectively. (e) Temporal waveform of the output signal under different bias voltages.

consisting of two 100-fs-wide pulses separated by 500 fs is shown in Fig. 8(a) and the signal through the dispersive element is shown in Fig. 8(b). The pump with 100-fs-wide pulse is shown in Fig. 8(c) and the pump through the dispersive element is shown in Fig. 8(d).

The signal at 1520 nm through the dispersion module depicted by the blue curve and the pump at 1555 nm through the dispersion module depicted by the black curve are combined into a coupler presented in Fig. 9(a). They are then sent into a 1-mm-long graphene-related waveguide with a cross-sectional size of 4×4 μm^2. The idler at 1590 nm is generated via the FWM process, which is picked out by a band-pass filter and shown in Fig. 9(b). The output signal is obtained after the idler has propagated through a dispersion compensation module equivalent to 100 km of dispersion compensation single mode fiber spools, and is presented in Fig. 9(b). Comparing the input signal shown in Fig. 8(a) with the output signal shown in Fig. 9(c), a magnification factor of 1000$\times$ for a signal consisting of two 100-fs-wide pulses separated by 500 fs is demonstrated. To the best of our knowledge, this is the first time 1000$\times$ magnification has been realized in a TIS. Moreover, based on the parameters of the proposed graphene-covered silicon nitride waveguide and the regular loss rule under different Fermi levels,[39,40] we have developed an electrically tunable TIS and determined the variation regularity of temporal amplification to the ultrafast pulse and the impact of mode field by adjusting the Fermi level of the graphene, as shown Fig. 10. As we can see from Figs. 10(a)–10(d), the mode field exhibits slight change. However, the temporal waveform of the output signal presents obvious differences under different Fermi levels of the graphene. As mentioned previously in this manuscript, the shift in bias voltage (Fermi level) changes the dispersion of the waveguide, which has a significant influence on conversion efficiency and the shape of pulses. It contributes to the tunability of the TIS. These results could promote the signal bandwidth from GHz to THz and give rise to practical applications in ultrafast optical signal processing.

In this work, a novel graphene-related waveguide model is proposed and the performance of different dimensions of silicon nitride on second-order dispersion characteristics under different bias voltages are investigated in detail. Furthermore, an electrically tunable TIS is realized based on the waveguide, which could work in a large wavelength range of about 700 nm in the near infrared region and present 1000$\times$ magnification of two 100 fs pulses separated by 500 fs. It allows for measuring signals with THz bandwidth using a detector with GHz bandwidth. These results provide significant reference for further research into temporal processing, with attractive potential for use in high-speed optical signal processing, integrated optics and ultrafast optics.

Acknowledgments This work was supported by the Strategic Priority Research Program of the Chinese Academy of Sciences (Grant No. XDB24030600) and China Scholarship Council.

1) B. H. Kolner, IEEE J. Quantum Electron. **30**, 1951 (1994).
2) M. T. Kauffman, W. C. Banyal, A. A. Godll, and D. M. Bloom, Appl. Phys. Lett. **64**, 270 (1994).
3) M. A. Foster, R. Salem, D. F. Geraghty, A. C. Turner-foster, M. Lipson, and A. L. Gaeta, Nat. Lett. **456**, 81 (2008).
4) C. V. Bennett, R. P. Scott, and B. H. Kolner, Appl. Phys. Lett. **65**, 2513 (1994).
5) R. Salem, M. A. Foster, A. C. Turner, D. F. Geraghty, M. Lipson, and A. L. Gaeta, Opt. Lett. **33**, 1047 (2008).
6) Y. K. Chembo, A. Hmima, P.-A. Lacourt, L. Larger, and J. M. Dudley, J. Lightwave Technol. **22**, 5160 (2009).
7) J. V. Howe and C. Xu, J. Lightwave Technol. **24**, 2649 (2006).
8) M. Karpinski, M. Jachura, L. J. Wright, and B. J. Smith, Nat. Photon. **228**, 1 (2016).
9) D. J. Moss, R. Morandotti, A. L. Gaeta, and M. Lipson, Nat. Photon. **183**, 597 (2013).
10) J. Schroder, F. Wang, A. Clarke, E. Ryckeboer, M. Pelusi, M. A. F. Roelens, and B. J. Eggleton, Opt. Commun. **283**, 2611 (2010).
11) B. H. Kolner, Opt. Lett. **14**, 630 (1989).
12) Y. Okawachi, R. Salem, M. A. Foster, A. C. Foster, M. Lipson, and A. L. Gaeta, Opt. Express **17**, 5691 (2009).
13) A. Pasquazi, M. Peccianti, Y. Park, B. E. Little, S. T. Chu, R. Morandotti, J. Azana, and D. J. Moss, Nat. Photon. **5**, 618 (2011).
14) L. K. Mouradian, F. Louradour, V. Messager, A. Barthelemy, and C. Froehly, IEEE J. Quantum Electron. **36**, 795 (2000).
15) M. A. Foster, R. Salem, Y. Okawachi, A. C. Foster, M. Lipson, and A. L. Gaeta, Nat. Photon. **3**, 581 (2009).
16) Y. Okawachi, R. Salem, A. R. Johnson, K. Saha, J. S. Levy, M. Lipson, and A. L. Gaeta, Opt. Lett. **37**, 4892 (2012).
17) A. Pasquazi, Y. Park, S. T. Chu, B. E. Little, F. Legare, R. Morandotti, J. A. Zana, and D. J. Moss, IEEE J. Quantum Electron. **18**, 629 (2012).
18) H. Hu et al., Opt. Express **19**, 19886 (2011).
19) D. Ansell, I. P. Radko, Z. Han, F. J. Rodrigue, S. I. Bozhevolnyi, and A. N. Grigorenko, Nat. Commun. **10**, 1 (2015).
20) X. Gan, R.-J. Shiue, Y. Gao, L. Meric, T. F. Heinz, K. Shepard, J. Hone, S. Assefa, and D. Englund, Nat. Photon. **7**, 883 (2013).
21) A. V. Rozhkov, G. Giavaras, Y. P. Bliokh, V. Freilikher, and F. Nori, Phys. Rep. **503**, 77 (2011).
22) H. Li, Y. Anugrah, S. J. Koester, and M. Li, Appl. Phys. Lett. **101**, 111110 (2012).
23) R. R. Nair, P. Blake, A. N. Grigorenko, K. S. Novoselov, T. J. Booth, T. Stauber, N. M. R. Peres, and A. K. Geim, Science **320**, 1308 (2008).
24) K. F. Mak, M. Y. Sfeir, Y. Wu, C. H. Lui, J. A. Misewich, and T. F. Heinz, Phys. Rev. **101**, 196405 (2008).

25) K. I. Bolotin, K. L. Sikes, Z. Jiang, M. Klima, G. Fudenberg, J. Hone, P. Kim, and H. L. Stormer, Solid State Commun. **146**, 351 (2008).
26) M. Liu, X. B. Yin, E. Ulin-Avila, B. S. Geng, T. Zentgraf, L. Ju, and X. Zhang, Nature **474**, 65 (2011).
27) M. Liu, X. B. Yin, and X. Zhang, Nano Lett. **12**, 1482 (2012).
28) Y. Meng, S. W. Ye, Y. J. Shen, Y. M. Yang, and M. L. Gong, IEEE Photonics J. **10**, 6600217 (2018).
29) Y. Meng, F. Hu, Y. J. Shen, Y. M. Yang, and M. L. Gong, Sci. Rep. **8**, 13362 (2018).
30) A. A. Balandin, S. Ghosh, W. Bao, I. Calizo, D. Teweldebrhan, F. Miao, and C. N. Lau, Nano Lett. **8**, 902 (2008).
31) G. W. Hanson, J. Appl. Phys. **103**, 064302 (2008).
32) X. Hanliang and X. Ling'an, Prog. Nat. Sci. **11**, 67 (2001).
33) Z. Song, H. Liu, N. Huang, and Z. Wang, J. Phys. D: Appl. Phys. **51**, 095108 (2018).
34) Z. Lu and W. Zhao, J. Opt. Soc. Am. B **29**, 1490 (2012).
35) C. Xu, Y. Jin, L. Yang, J. Yang, and X. Jiang, Opt. Express **20**, 22398 (2012).
36) P. Xie, Q. Sun, L. Wang, Y. Wen, X. Wang, G. Wang, C. Zeng, M. Liu, Z. Ge, and Z. Lu, Appl. Phys. Express **11**, 082204 (2018).
37) C. G. Durfee, A. R. Rundquist, S. Backus, C. Herne, M. M. Murnane, and H. C. Kapteyn, Phys. Rev. Lett. **83**, 2187 (1999).
38) L. An, H. Liu, Q. Sun, N. Huang, and Z. Wang, Appl. Opt. **53**, 4886 (2014).
39) K. Alexander, N. A. Savostianova, S. A. Mikhailov, D. V. Thourhout, and B. Kuyken, ACS Photonics **5**, 4948 (2018).
40) J. Q. Wang, Z. Z. Cheng, C. Shu, and H. K. Tsang, IEEE Photonics Technol. Lett. **27**, 1765 (2015).